

# Changes in Surface Urban Heat Island Effect with the Development of New Towns

**Kyungil Lee**

Korea University

**Yoonji Kim**

Korea University

**Hyun Chan Sung**

Korea University

**Seung-Hee Kim**

Chapman University

**Seong Woo Jeon** (✉ [eepps\\_korea@korea.ac.kr](mailto:eepps_korea@korea.ac.kr))

Korea University

---

## Research Article

**Keywords:** thermal research, climate, urban heat islands, Pangyo, urbanisation

**Posted Date:** May 13th, 2021

**DOI:** <https://doi.org/10.21203/rs.3.rs-515349/v1>

**License:**  This work is licensed under a Creative Commons Attribution 4.0 International License.

[Read Full License](#)

---

# Changes in surface urban heat island effect with the development of new towns

Kyungil Lee<sup>1</sup>, Yoonji Kim<sup>1</sup>, Hyun Chan Sung<sup>1</sup>, Seung Hee Kim<sup>2</sup>, and Seong Woo Jeon<sup>1\*</sup>

<sup>1</sup>Division of Environmental Science & Ecological Engineering, Korea University, 02841 145 Anam-ro, Seongbuk-gu, Seoul, 02841

<sup>2</sup>Center of Excellence in Earth Systems Modeling and Observations, Chapman University, Orange, CA 92866, USA.

## Abstract

A new town is a planned and built within a relatively short period compared to existing cities. It is suitable for climate and thermal research, particularly formulating urban planning strategies to analyse problems such as urban heat islands (UHIs). Herein, a comprehensive approach was demonstrated for determining changes in surface UHI (SUHI) distribution during 1989–2048 in two new towns with different urban planning. A significant increase in built-up areas was observed from 1989 (< 5%) to 2018 (> 40%) in both new towns. However, the areas where SUHIs occurred before and after development increased further (approximately 12.25%) in Bundang new town where the green area ratio was lower and the building density was higher. However, in terms of SUHI intensification, the building structure of Pangyo new town, which has a lower floor area ratio, was analysed to be more suitable. Moreover, without effective mitigation, the built-up area in each new town is estimated to increase to approximately 60%, and the SUHI intensity in most areas to increase by 4 °C in 2048. Thus, these results combined with architectural assessment models can improve the understanding of thermal environmental impacts of urbanisation and help mitigate urban thermal hazards.

Global population growth and urban expansion primarily cause land use and land cover (LULC) changes and increases in built-up area. In 2018, approximately 55.3% of the world's population resided in cities, among which 60% will reside in cities with approximately 0.5 million inhabitants by 2030<sup>1</sup>. Rapidly increasing economic development accelerates these changes, particularly in fast-growing urban areas, hindering sustainable development<sup>2</sup>. LULC changes induced by human activities lead to different local climates than in surrounding areas. This effect, termed as urban heat island (UHI), occurs worldwide<sup>3,4</sup>. UHIs primarily occur due to increased solar radiation absorption and trapping in new surface materials of various infrastructure<sup>5,6</sup>. The magnitude and extent of UHIs are highly positively correlated with urban area and population size in cities;

29 thus, UHIs are significantly affected by urban expansion<sup>7</sup>. UHIs can be divided into two types: meteorological  
30 UHI, an increase in local air temperature<sup>8</sup>, and surface urban heat island (SUHI), an increase in urban skin  
31 temperature<sup>9</sup>. SUHI is particularly evident in spatial variations of upwelling thermal radiance caused by LULC  
32 changes and is commonly influenced by the surrounding sub-urban environment<sup>8,9</sup>.

33 A new town, also called planned city, is built in a short period within a pre-determined boundary for  
34 specific purposes. Since the mid-to-late twentieth century, new towns have been constructed worldwide,  
35 contributing to population growth and inflation in large cities<sup>10,11</sup>. New towns facilitate climate and thermal  
36 research through formulation of urban planning strategies to analyse problems, such as UHIs, and by providing  
37 information on the urban temporal temperature variation mechanism<sup>12</sup>. Comparison of UHI changes in new  
38 towns have not yet been conducted. Carrying out comparative studies on climate effects of urbanisation under  
39 different urban planning conditions is particularly difficult because of different urban environments, economic  
40 situations, and climates, as well as inconsistent data.

41 Since 1990, 14 new towns have been repopulated or built in sub-urban areas in South Korea to manage  
42 population, transportation, and environmental concerns in several large cities. Urban planning in the first-  
43 generation new towns, providing indiscriminate housing, was not systematic and resulted in negative impacts,  
44 such as unplanned urban expansion, environmental degradation, and low greenspace ratio in housing complexes.  
45 The second-generation new towns were developed through systematic and environmentally friendly urban  
46 planning, such as low-density urbanisation and expansion of green areas (Table 1). However, in both cases, an  
47 increase in UHI is estimated because of a rapid infrastructural development and vegetation loss. Moreover, the  
48 UHI phenomenon may intensify with further urban expansion.

49 Herein, expansion and intensification of UHI due to new town development was empirically analysed  
50 using satellite data in two different-generation new towns in South Korea (Fig. 1). The SUHI intensity of each  
51 new town is the difference between the temperatures of built-up and surrounding areas within the boundary<sup>4,13-</sup>  
52 <sup>15</sup>. A Markov chain model, combined with the cellular automata method, determined the SUHI distribution with  
53 LULC changes in the two new towns. Notably, urban planning influenced the change patterns in the expansion  
54 and intensification of UHIs, despite urban expansion. Furthermore, the future SUHI intensities in new towns  
55 may significantly increase with changes in structural characteristics owing to renovation and additional urban  
56 expansion.

## 57 **Results**

58 **LULC changes according to new town development.** In the accuracy assessment of the three LULC  
59 classifications, the kappa coefficient in LULC classification areas for all the three years were greater than 0.8,  
60 verifying that these classifications were significant predictors of future LULC and SUHI distribution. LULC  
61 analysis showed that the extent and proportion of LULC types varied temporally, and significant  
62 transformations were observed between 1989 and 2018. The accumulation of built-up areas in the two new  
63 towns has been significantly increased during each development period (Fig. 2b and Fig. 3b). However, forest  
64 and agricultural areas had significantly declined. In 1989, most of the LULCs in Bundang new town and Pangyo  
65 new town were forest and agricultural areas, accounting for approximately 85% of the total area, while built-up  
66 areas accounted for less than 5%. After that, the highest built-up growth occurred in Bundang new town  
67 between 1989 and 2000, when the development phase of Bundang new town was over. The built-up areas  
68 increased from 1.47 km<sup>2</sup> (4.39%) to 14.09 km<sup>2</sup> (42.13%); however, agricultural areas significantly decreased  
69 from 13.90 km<sup>2</sup> (41.55%) to 2.99 km<sup>2</sup> (8.93%), and forests also considerably decreased from 44.19% to 33.88%.  
70 In addition, open spaces increased from 0.46% to 5.68%, which was due to the development of the new town, or  
71 because it was an area under development at that time (Fig. 2a). In Pangyo new town, very little change had  
72 occurred because new town development planning was not yet established. In the case of built-up areas, the  
73 proportion increased from 3.23% to 16.73%, which was confirmed by the construction of the main road within  
74 the boundary and unplanned and fragmented development (Fig. 3a). This also evidently increased the  
75 percentage of open spaces in this process.

76 In 2018, when the development of Pangyo new town was completed, the proportion of built-up areas in  
77 this new town considerably increased from 16.73% to 40.81%. Forest areas decreased from 8.17 km<sup>2</sup> (46.38%)  
78 to 7.20 km<sup>2</sup> (40.84%) and the remaining agricultural areas decreased to 1.96%, resulting in almost complete  
79 urbanisation. In the case of Bundang new town, urban expansion occurred through additional urban  
80 development and partial renovation between 2000 and 2018. The proportion of built-up areas increased by 7%  
81 but agricultural areas decreased by 1.71% (0.57 km<sup>2</sup>); indicating almost complete urbanisation. Open spaces that  
82 existed in both new towns in 2000 were also mostly urbanised in 2018. Due to the low resolution of images, the  
83 grass in the built-up areas could not be classified, but the proportion of grass was higher in Pangyo new town  
84 than in Bundang new town as recorded during urban planning. The actual ratio between the two new towns  
85 would be different. In the case of water bodies, there was no significant change in the areas between 1989 and  
86 2018, but fluctuations due to spectroscopic differences were observed.

87 **SUHI distribution changes according to new town development.** The accumulation of higher SUHI  
88 intensity areas in both the new towns had increased with urban expansion (Fig. 2d and Fig. 3d). In 1989, there  
89 were no areas in both Bundang and Pangyo new towns with a SUHI intensity of six or higher. Most of the areas  
90 with evident SUHI phenomenon were agricultural areas and partially urbanised areas. Land surface temperature  
91 (LST) is sensitive to vegetation mass, and in Korea, May is an early growing season in agricultural areas that  
92 contain less vegetation mass compared to the surrounding forest<sup>16</sup>. This difference in vegetation mass led to a  
93 high temperature distribution in agricultural areas in both new towns. In 2000, the area with SUHI phenomenon  
94 increased by approximately 30% after the development of Bundang new town. The areas with SUHI occurrence  
95 in the range of 2 °C–4 °C significantly increased from 3.4 km<sup>2</sup> (10.18%) to 10.82 km<sup>2</sup> (32.34%), and those with  
96 more than 4 °C, which were few in 1989, increased to approximately 3.03 km<sup>2</sup> (9%) of the total area. In the case  
97 of Pangyo new town, the areas with the SUHI phenomenon increased by approximately 6.5%, and most of these  
98 were distributed across the built main road and surrounding areas. The area with SUHI occurrence in the range  
99 2 °C–4 °C increased from 1.77 km<sup>2</sup> (10.06%) to 3.23 km<sup>2</sup> (18.33%), and those with more than 4 °C were less  
100 than 0.324 km<sup>2</sup> (2%) (Fig. 2c). Compared to the developed Bundang new town, Pangyo new town showed a  
101 smaller overall increase in the SUHI phenomenon.

102 In 2018, when the development of Pangyo new town was completed, the areas experiencing the SUHI  
103 phenomenon increased by approximately 17%. The areas with SUHI occurrence in the range 2 °C–4 °C  
104 increased from 3.23 km<sup>2</sup> (18.33%) to 4.68 km<sup>2</sup> (26.58%), and those in the range 4–6 °C significantly increased  
105 from 0.32 km<sup>2</sup> (1.81%) to 2.51 km<sup>2</sup> (14.23%). However, few areas were found that had temperatures greater  
106 than 6 °C, and none exceeded 8 °C. For Bundang new town, the areas with SUHI < 2 °C had decreased, and the  
107 areas with higher SUHI intensity had increased overall. The areas with SUHI in the range 4 °C–6 °C increased  
108 from 2.76 km<sup>2</sup> (8.25%) to 3.69 km<sup>2</sup> 11.03%, and those with more than 6 °C increased to approximately 2% of  
109 the entire new town. This implied that the increase in building density and building renovation through  
110 additional development may be the main causes of the intensified SUHI phenomenon in existing cities (Fig. 3c).  
111 Buildings are responsible for more than 40% of the global energy consumption, and structural characteristics are  
112 related to the UHI intensity<sup>17,18</sup>. Renovation for outdated buildings, such as extension and new construction,  
113 intensify the UHI phenomenon<sup>18</sup>. The increase in total area and intensity of the SUHI phenomenon before and  
114 after Pangyo new town development was evidently lower than that of Bundang new town. However, the area  
115 with SUHI in the range of 4 °C–6 °C increased higher than that of Bundang new town. This may also be due to

116 differences in structural characteristics, floor area ratio, and height of buildings built in new town. The floor area  
117 ratio of buildings in Bundang new town is higher than in Pangyo new town.

118 Building floor ratio means the sum of the gross horizontal area of each floor of a building as measured to  
119 the exterior face of the exterior walls of the building. According to Oke et al. (2017)<sup>14</sup>, the facet surface  
120 temperature in daytime in urban system is typically ranked as follows:  $T_{\text{roof}} > T_{\text{walls}} > T_{\text{floor}} > T_{\text{surrounding area}}$ . In  
121 addition, in canyons formed in the city through high-rise buildings, overshadowing areas are formed to induce  
122 surface coolness<sup>60</sup>. As a result, it was found that buildings newly built in Pangyo new town, which have a lower  
123 height than Bundang new town and a certain level of building coverage ratio, are more suitable for increasing  
124 surface temperature.

125 **Predicted LULC for 2028, 2038, and 2048.** The cellular automata (CA)-Markov chain model (MCM)  
126 analysis predicted that the proportion of built-up areas would increase by approximately 10% from 16.44 km<sup>2</sup>  
127 (49.16%) to 19.78 km<sup>2</sup> (59.12%) between 2018 and 2048 in Bundang new town (Fig 2a). Moreover, it predicted  
128 decreases in forest areas from 35.61% to 29.9% and the grass cover from 12.76% to 10.69%. As new town  
129 development in the past primarily occurred through transformation of agricultural areas to built-up areas, it was  
130 not predicted that a significant urban expansion would occur through deforestation. In addition, most of the  
131 buildings in the housing complex of Bundang new town were completed in 1990, over 25 years ago. Therefore,  
132 renovations are planned for most of these old apartment complexes to improve the poor residential environment  
133 and meet the latest urban housing requirements. Hence, most urban expansion was predicted to occur through  
134 renovation within the existing built-up areas and partial transformation of the forest surrounding the new town.

135 In the case of Pangyo new town, the proportion of urban expansion between 2018 and 2048 was  
136 predicted to be higher than that of Bundang new town. According to the CA-MCM prediction, built-up areas  
137 would increase by approximately 18.42% from 40.81% to 59.23%, the forest areas would decrease from 40.84%  
138 to 32.25%, and the grass cover including golf courses would decrease from 15.34% to 7.92% (Fig. 3a). The  
139 primary trend observed in the predicted urban expansion was that non-urban areas, such as forest and grass,  
140 surrounding the main road were transformed into built-up areas. In contrast with Bundang new town, Pangyo  
141 new town is public-transportation-oriented. During the past new town development, the areas surrounding the  
142 main road that existed outside the city were underdeveloped. However, if urban expansion occurs in the future,  
143 it would be evident primarily in areas with good road proximity. In addition, urban expansion due to the  
144 completion of development in the open spaces that were under development in 2018, and further development

145 within the city was also predicted. In terms of agricultural area and water, both new towns were predicted to  
146 remain almost unchanged from 2018, with little fluctuation.

147 **Predicted SUHI distribution for 2028, 2038, and 2048.** CA-MCM predicted the increase in area and  
148 intensity of the SUHI phenomenon in both new town and, unlike LULC prediction, a significant change was  
149 predicted. In Bundang new town, the areas where the SUHI phenomenon occurs would increase by  
150 approximately 5% between 2018 and 2048. For SUHI intensity distribution, the areas with  $SUHI \leq 4$  °C would  
151 decrease from 17.12 km<sup>2</sup> (51.16%) to 11.44 km<sup>2</sup> (34.21%). Simultaneously, the areas with  $SUHI > 4$  °C was  
152 estimated to increase from 4.25 km<sup>2</sup> (12.73%) to 10.68 km<sup>2</sup> (34.71%), affecting the lower SUHI intensity areas.  
153 It is predicted that SUHI intensity would expand and increase from the existing residential area, which may  
154 reflect the renovation trend partially occurring between 2000 and 2018. Therefore, development of sustainable  
155 renovation guidelines is required such as thermal insulation, replacement of the insulation material, and  
156 improving the air tightness of the building envelope through renovation using insulation materials<sup>19</sup>. In addition,  
157 the areas with  $SUHI > 6$  °C are predicted to increase from 0.56 km<sup>2</sup> (1.7%) to 2.77 km<sup>2</sup> (8.28%). It has been  
158 observed that the higher the LST, the higher the frequency of heat waves at regional scales<sup>20</sup>. In the future,  
159 additional thermal environmental policies and energy policies are required for areas where SUHI intensity is  
160 expected to increase significantly (Fig. 3a).

161 In the case of Pangyo new town, the areas where the SUHI phenomenon occurred were predicted to  
162 increase by 20%. The affected areas are similar to those predicted to change from forests existing around the  
163 main road to built-up areas. For SUHI intensity distribution, the area with  $SUHI \leq 4$  °C would decrease from  
164 7.75 km<sup>2</sup> (43.97%) to 5.08 km<sup>2</sup> (28.83%). Moreover, the areas with  $SUHI > 4$  °C would increase from 2.53 km<sup>2</sup>  
165 (14.34%) to 8.7 km<sup>2</sup> (49.36%), and most areas were in the range 4 °C–6 °C (49%) (Fig. 3c). Therefore, it can be  
166 predicted that urban features, such as structural characteristics, materials, and building disposition type would  
167 change according to the housing complex newly built through new town development.

## 168 **Discussion**

169 This study is the first attempt to simulate and compare the pattern of UHI occurrence according to new town  
170 development using remote sensing and GIS technology. This discussion focuses on the principal two  
171 contributions of the proposed research in comparison with previous studies. Afterwards, the limitations are  
172 discussed.

173           The main contribution of our study is that the different patterns of changes in land use land cover and  
174 SUHI phenomenon depending on urban planning were visually and quantitatively shown for the study sites  
175 excluding external influences. To provide some examples, Tran et al.<sup>7</sup> and Clinton&Gong<sup>8</sup> do comparative  
176 analysis of SUHI phenomenon between cities under different environment or urban situation. Tran et al.<sup>7</sup>  
177 examine the spatial patterns of SUHIs for Asian mega cities based on the season and relationship with surface  
178 properties. Clinton&Gong<sup>8</sup> estimate the magnitude of SUHI for urban areas between latitudes 71 and – 55 for  
179 the year 2010 using MODIS datasets. The results of these studies were successful in demonstrating the  
180 contribution of urbanization to the SUHI effect as well as investigating the differences in SUHI between urban  
181 and surrounding areas. However, applying these methods could not provide insight into the effect of different  
182 urban development types or urban planning on UHI phenomenon. In addition, in terms of comparing the UHI  
183 phenomenon between cities, there were some limitations which may lower the reliability of comparison. They  
184 all used satellite images constructed at different times and the magnitude of SUHI depends on whether a single  
185 image or composite over a period of time is used<sup>14</sup>. In comparison with these previous studies, this research  
186 provides a significant contribution by quantifying the influence of the urban planning involved in the UHI  
187 phenomenon based on a scientific approach in condition which external influences are controlled. The  
188 developed LULC maps showed significant changes in LULC before and after the development of new town  
189 from 1989 to 2018. The primary driver for the development of both the new towns was the transformation of  
190 agricultural areas to built-up areas. Moreover, the increase in built-up areas evidently intensified the SUHI  
191 phenomenon of an entire new town. However, the areas where the SUHI phenomenon additionally occurred or  
192 the SUHI intensity increased, were different according to the urban plan. These differences indicated the  
193 requirement and importance of urban planning to maintain a sustainable thermal environment, even with rapid  
194 LULC changes.

195           Our research also improves on the predictive models previously developed to study and predict usually  
196 LULC patterns. Unlike previous studies, Cellular Automata Markov Chain model was used for prediction of  
197 LULC changes and SUHI distribution changes accordingly in study areas. In the case of existing studies, the  
198 LULC change was simply predicted using the same model, but there was a limitation in not examining the urban  
199 climate change or other possible effects<sup>24,45-47</sup>. Saha et al.<sup>22</sup> and Tariq&Shu<sup>57</sup> tried to examine the LST change  
200 according to the LULC change. However, it did not predict the change of the LST distribution according to the  
201 predicted future LULC, and as in previous studies, indirect prediction was performed by simply constructing a  
202 regression equation using the spectral index. In addition, the LST value may vary depending on the radiative and

203 aerodynamic properties of the satellite image and it is difficult to confirm the relative temperature increase in the  
204 built-up areas according to urban growth using LST distribution<sup>14</sup>. In this study, the predicted results based on  
205 variations between 2000 and 2018 also showed a possible future pattern of further urban expansion and similar  
206 changes in SUHI distribution and intensity in both new towns.

207 In addition, through prediction analysis, the importance of building renovation and structural  
208 characteristics in urban-level thermal environment changes was also suggested. According to Yahia et al.,  
209 (2018)<sup>60</sup>, closely spaced high-rise buildings have a negative impact on ventilation and the average wind speed in  
210 the dense high-rise buildings area is less than half of that of the low-rise buildings area. However, when  
211 comparing the physiologically equivalent temperature, high-rise buildings is more comfortable, and the shade  
212 seems to be more important factor than wind speed. It means that decreasing solar radiation through shade will  
213 have a greater effect on decreasing sensible heat and thermal comfort near the surface than promoting the wind  
214 speed. When renovating old buildings in the future, three-dimensional design considering the effects of shadow  
215 and wind at the same time are required.

216 While the presented study provides useful method and information regarding the current and future status  
217 of the UHI phenomenon, it is still faced some limitations. This study does not consider additional parameters  
218 typically influencing the urban growth because of the specificity of the study area. As mentioned, new town is  
219 the planned city where the physical and legal aspects of the site were reviewed through feasibility analysis  
220 beforehand, the complication associated with urban expansion is relatively low for new town. However, the  
221 factors for urbanisation are related to the complexity of the terrain, degree of socio-economic development,  
222 urban regulations, etc<sup>24</sup>. Therefore, it is necessary to consider additional factors for urban expansion when  
223 applying this methodology to a region other than new town in the future. In addition, a model that explains the  
224 detailed behaviour of UHI using a combination of building renovation and structural characteristics is still  
225 necessary. Future research studies should attempt to obtain structural and temporal data over the same period of  
226 time and develop models able to explain the change of UHI based on structural characteristics changed by  
227 building renovation.

## 228 **Conclusions**

229 Although the research methods and measures face certain conceptual and practical challenges, this study  
230 suggested a proximate causal relationship between urban expansion and SUHI phenomenon change according to  
231 urban planning. It is easy to apply for practitioners and the necessary data for application are available without

232 complex acquisition procedures or unopened access datasets. Therefore, the proposed novel method may be  
233 applied to both existing and newly built cities to predict future UHI distribution according to urban planning.  
234 Furthermore, the findings and methods constructed through this research can be useful to policy makers, urban  
235 planners, researchers, and citizens to adopt sustainable thermal environment management practices including  
236 adaptation and mitigation strategies for the city.

## 237 **Methods**

238 **Data acquisitions and pre-processing.** Three Landsat images from May with an image quality of nine and  
239 cloud cover less than 2% were used to minimise the seasonal influence and cloud cover of each period: 1989,  
240 2000, and 2018. Two Landsat 5 thematic mapper (TM) and one Landsat 8 operational land imager/thermal  
241 infrared sensor (OLI/TIRS) images were obtained from the United States Geological Survey - Centre for Earth  
242 Resources Observation and Science (USGS-EROS) (<http://earthexplorer.usgs.gov/>). The images were used for  
243 LULC classification and SUHI calculation, and each period showed the change trends before and after the new  
244 town development. The remotely sensed data is an indirect measurement considering the intervening  
245 atmosphere and the surface radiative properties that influence the emission and reflection of radiation within the  
246 spectral wavelengths detected by the sensor<sup>9</sup>. Atmospheric correction using the dark object subtraction (DOS)  
247 method and radiometric correction for pre-processing using the semi-automatic classification (SCP) plugin in  
248 QGIS 3.14, were applied to the images. Atmospheric scattering and absorption caused the imaging system to  
249 record a non-zero digital number (DN) value for dark objects. The DOS method subtracted the constant non-  
250 zero DN value, DN haze, from the whole band, if some objects under complete shadow must have zero  
251 reflectance<sup>21</sup>.

252 **Land use land cover classification.** A supervised classification technique was used with the maximum  
253 likelihood classifier (MLC) algorithm to generate LULC maps for each year using the SCP plugin in QGIS 3.14.  
254 The MLC-based supervised classification approach was comprehensively used and considered as an established  
255 technique in many previous studies for urban LULC classification, where the spatial heterogeneity of pixels is  
256 similarly high<sup>22-24</sup>. The MLC algorithm is based on probability density distribution functions (likelihood),  
257 includes all training inputs for each land cover class, and has been proven to be an accurate and robust algorithm  
258 because it does not overestimate the class values during the computational process<sup>23-25</sup>. In addition, there are  
259 some advantages of the MLC algorithm, such as (1) auto-allocation of pixels to the unclassified regions based  
260 on the surrounding values<sup>25</sup>, and (2) the variance and covariance values of the class signatures are considered

261 within the class distribution<sup>26</sup>. The Landsat images of 1989, 2000, and 2018 were classified into six major  
 262 LULC classes, (i) built-up areas, covering the buildings and concrete areas; (ii) forest, covering coniferous and  
 263 broadleaf forests; (iii) grass, covering natural and artificial grass; (iv) open spaces, covering natural and artificial  
 264 bare areas; (v) agricultural areas, covering paddy field, dry field, etc.; and (vi) water bodies, covering ponds,  
 265 lakes, and wetlands.

266 Assessment of classification accuracy is necessary to ensure that classification data can detect changes;  
 267 this was conducted on the resulting classified imagery through an error matrix and kappa index that enables  
 268 differentiation between ground-truth and predicted classification<sup>24,27</sup>. High-resolution Google Earth data and  
 269 aerial photographs provided by the National Geographic Information Institute (NGII) of South Korea were used  
 270 to establish ground-truth regions for the evaluation of classification accuracy (<http://map.ngii.go.kr/>). High-  
 271 resolution data from Google Earth have been used as reference in many classification studies and national  
 272 standardised land cover maps; NGII provides high-resolution aerial photographs captured since 1945, and can  
 273 also be used for accuracy assessment<sup>22,24,28</sup>. The kappa coefficient was calculated using equation (1):

$$kappa - coefficient = \frac{n \sum_{i=1}^k n_{ii} - \sum_{i=1}^k (G_i C_i)}{n^2 - \sum_{i=1}^k (G_i C_i)} \quad (1)$$

274 where  $i$  is the class number;  $n$  is the total number of points;  $n_{ii}$  is the number of pixels belonging to the actual  
 275 data class  $i$ , which were classified as class  $i$ ;  $C_i$  is the total number of classified pixels belonging to class  $i$ ; and  
 276  $G_i$  is the total number of actual data belonging to class  $i$ . Fifty sample points per class for each new town, except  
 277 water class, were selected automatically by QGIS 3.14. A minimum of 50 samples must be collected for each  
 278 land cover class in the error matrix to avoid the risk of a biased sample during accuracy assessment<sup>29</sup>.

279 **LST estimation.** LST estimation using ArcMap 10.5 includes transforming DNs to radiance ( $L_\lambda$ ), measuring  
 280 radiance brightness temperatures ( $T_B$ ), and adjusting emissivity to extract surface temperature from brightness  
 281 maps<sup>30</sup>. The LST values were obtained using thermal bands from Landsat TM (B6) and Landsat OLI/TIRS  
 282 (B10) because of the USGS recommendation to avoid using TIRS band 11 because of its higher calibration  
 283 uncertainty.

284 Every object on the Earth emits thermal electromagnetic radiation when its temperature is above absolute  
 285 zero (K), and the signal received by the thermal sensors can be transformed to radiance ( $L_\lambda$ ) using equation (2):

$$L_{\lambda} = M_L \times Q_{CAL} + A_L \quad (2)$$

286 where  $L_{\lambda}$  is the spectral radiance in  $W/(m^2 \times sr \times \mu m)$ ;  $M_L$  is the radiance multiplicative scaling factor for the band;  
 287  $A_L$  is the radiance additive scaling factor for the band; and  $Q_{cal}$  is the level 1 pixel value in DN, whose values are  
 288 obtained from the metadata of the Landsat images. After the DN value was converted to radiance, the radiance  
 289 values were converted to  $T_B$  using equation (3):

$$T_B = K_2 / \ln[(K_1 / L_{\lambda}) + 1] - 273.15 \quad (3)$$

290 where  $T_B$  is the At-satellite brightness temperature and  $K_1$  and  $K_2$  represent the band-specific thermal conversion  
 291 constants from the metadata. To obtain the temperature in Celsius, the radiant temperature is revised<sup>30</sup>. The final  
 292 step in estimating the LST is to rectify the TB using land surface emissivity (LSE,  $\epsilon$ ) correction as shown in  
 293 equation (4)<sup>31</sup>:

$$LST = \frac{T_B}{[1 + \frac{\lambda \times T_B}{\rho} \times \ln \epsilon]} \quad (4)$$

294 where  $\lambda$  is the wavelength of the emitted radiance ( $= 10.895 \mu m$ );  $\rho = h \times c / \sigma$  ( $1.438 \times 10^{-2} m K$ ), where  $h$  is  
 295 Planck's constant ( $6.626 \times 10^{-34} Js$ ),  $c$  is the velocity of light ( $2.998 \times 10^8 m/s$ ), and  $\sigma$  is the Boltzmann  
 296 constant ( $1.38 \times 10^{-23} J/K$ ); and  $\epsilon$  is the emissivity<sup>30,32</sup>.

297 The obtained values of  $T_B$  were referenced as a black body, whose properties are different from that of  
 298 real objects on the Earth's surface and would also be different from real LST<sup>33</sup>. The LST values across a city can  
 299 have a wide range, and it depends on LULC states constructed within the city. Furthermore, LSE, which is  
 300 essential for estimating the LST, has strong land use/land cover dependence<sup>34,35</sup>.

301 The LSE value is calculated conditionally using equation (5), and the condition is represented by the  
 302 formula for each emissivity value<sup>36,37</sup>:

$$\epsilon_{\lambda} = \epsilon_v P_v + \epsilon_s (1 - P_v) + C_{\lambda} \quad (5)$$

303 where  $\epsilon_v$  and  $\epsilon_s$  are the vegetation and soil emissivity, respectively and  $C_{\lambda}$  is the surface roughness ( $C = 0$  for  
 304 homogeneous and flat surfaces), with a constant value of  $0.005^{38}$ . When the normal difference vegetation index  
 305 (NDVI) is less than  $NDVI_s = 0.2$ , it is classified as bare soil and its emissivity value is acquired from the  
 306 reflectance values in the red region ( $\rho R$ )<sup>39</sup>. The NDVI values between 0.2 and 0.5 are considered as mixtures of

307 soil and vegetation surfaces, and equation (5) is used for extracting their emissivity values. In the equation,  $\epsilon_{\lambda v}$  is  
 308 the emissivity value of vegetation ( $= 0.9863 \mu\text{m}$ ) and  $\epsilon_{\lambda s}$  is emissivity value of soil ( $= 0.9668 \mu\text{m}$ ) in this  
 309 range<sup>40</sup>. When the NDVI value is larger than  $\text{NDVI}_v = 0.5$ , it is considered as a vegetation surface and an  
 310 emissivity value of 0.99 is assigned to it<sup>30</sup>. Visible red and near-infrared (NIR) bands were used for calculating  
 311 NDVI using equation (6). In addition, NDVI values were used to evaluate the proportion of the vegetation ( $P_v$ )  
 312 related to emissivity ( $\epsilon$ ) using equation (7)<sup>41,42</sup>. A method for calculating  $P_v$  using the NDVI values for  
 313 vegetation soil, which can be applied in global conditions, was suggested in a previous study<sup>36</sup>.

$$NDVI = \frac{NIR - RED}{NIR + RED} \quad (6)$$

314

$$P_v = \left[ \frac{NDVI - NDVI_s}{NDVI_v - NDVI_s} \right]^2 \quad (7)$$

315 **Urban expansion prediction.** An integrated CA method combined with MCM was used for predicting urban  
 316 expansion in 2028, 2038, and 2048 under the business-as-usual scenario of both new towns. The CA-MCM is a  
 317 hybrid and robust algorithm in spatial and temporal dynamic modelling of LULC changes that includes the  
 318 deterministic modelling framework, spatially explicit approach with stochastically based temporal  
 319 framework<sup>43,44</sup>. In addition, CA-MCM analysis allows the user to add factors related to urban expansion into the  
 320 model to improve accuracy, and it can be a support tool for land use planners and policy makers to establish  
 321 future land use policies<sup>45</sup>. Furthermore, MCM is a tool used to evaluate adjustments in land use among cycles by  
 322 a sequence of values that depend on the present state<sup>46</sup>. MCM defines the present temporal LULC change to  
 323 predict future change, and equation (8) presents the calculation of land use change prediction<sup>47</sup>:

$$S(t, t + 1) = P_{ij} \times S(t) \quad (8)$$

324

325 where  $S(t)$  is the system state at time  $t$ ,  $S(t+1)$  is the system state at time  $t+1$ , and  $P_{ij}$  is the transition probability  
 326 matrix in a state, which is calculated using equation (9).

$$P_{ij} = \begin{bmatrix} P_{1,1} & P_{1,2} & \dots & P_{1,N} \\ P_{2,1} & P_{2,2} & \dots & P_{2,N} \\ \dots & \dots & \dots & \dots \\ P_{M,1} & P_{M,2} & \dots & P_{M,N} \end{bmatrix} \quad (0 \leq P_{ij} \leq 1) \quad (9)$$

327 P is the Markov probability matrix,  $P_{ij}$  is the probability of converting from current state  $i$  to another state  $j$  in  
328 prediction time, and  $P_N$  is the state probability of any time. Low transition pixels have a low probability value  
329 near (0), and high-transition pixels have a high probability value near (1)<sup>47</sup>. The 2000 LULC map of the study  
330 area was used as the first base ( $t_1$ ), and the 2018 LULC map was used as the other ( $t_2$ ) to obtain the transition  
331 probability matrix in this study. However, MCM cannot completely predict the LULC change because it does  
332 not consider spatial knowledge distribution within each category, and transition probabilities are not constant  
333 among LULC states; therefore, it may suggest the appropriate degree of change but not the appropriate  
334 direction<sup>48</sup>.

335 CA is a dynamic process model used for land use cover change<sup>45</sup>. CA has the ability to change its state  
336 according to the principle that each cell with its own characteristics can represent parcels of land and self-  
337 growth interactions as they are dynamic and can duplicate<sup>49</sup>. Land use changes for any location (cells) can be  
338 defined by the existing state and changes in the neighbouring cells, and the growth of objects is simulated in two  
339 directions<sup>45</sup>. Hence, CA-MCM, which incorporates the theories of Markov chain analysis and CA, has the  
340 advantages of forecasting in terms of utilising time series and space, and can achieve improved simulation for  
341 temporal and spatial patterns of land use changes<sup>50</sup>. Multi-criteria evaluation (MCE) was used to determine the  
342 LULC classes suitable for changing from the original state to another. MCE combines the factors driving urban  
343 growth and fuzzy systems analysis to construct transition suitability maps that show the probability that a pixel  
344 would change to another land cover class or remain unchanged<sup>51</sup>. The determinants and spatial expansion of  
345 urbanisation are related to the complexity of the terrain, degree of socio-economic development, urban  
346 regulations, etc<sup>24</sup>. However, in the case of new towns, as the physical and legal aspects of the site were reviewed  
347 through feasibility analysis, the complexity associated with urban expansion is relatively low.

348 In contrast, during urban planning in new town, physical planning and transportation infrastructure are  
349 more important for large-scale development to generate housing sites within a short period. Transportation  
350 infrastructure stimulates and guides urban growth by improving accessibility<sup>52-54</sup>. In addition, slope is an  
351 uncontrollable environmental factor that affects urban growth, because construction of buildings and  
352 development of cities on steep-slope terrain is difficult or sometimes impossible<sup>55</sup>. Hence, the distance to the  
353 main road, slope, and distance to the existing urban area were used to calculate transition suitability maps in this  
354 study. The maps of the road and digital elevation model (DEM) were obtained from National Spatial Data in  
355 Infrastructure Portal (NSDIP) (<http://data.nsdip.go.kr/>). Fuzzy membership functions were used to standardise  
356 suitability maps into 0–1, where 0 represents unsuitable locations and 1 represents ideal locations for

357 urbanisation. The area of each land class to be transformed into another LULC class was estimated based on the  
358 transition probabilities. These areas were separated by the number of iterations performed for CA to predict the  
359 areas to be converted per iteration. The future assignment of each cell to an LULC class was based on the  
360 suitability of the cell for that LULC class and the similarity of the cell with neighbouring cells of the same class.  
361 A contiguity filter of 5×5 pixels was used to define the effect of neighbouring pixels on the central pixel.

362 **Mapping and prediction of the SUHI distribution.** The UHI effect occurs due to the anthropogenic  
363 modification of natural landscapes in the city boundary layer, and as the urban area increases, the UHI intensity  
364 also increases<sup>14</sup>. In addition, LST and SUHI effects are particularly related to the surrounding sub-urban  
365 environment<sup>8,14</sup>. To analyse this trend, the SUHI intensity of each new town was defined as the difference  
366 between the temperatures of an urban area and its surrounding areas (LULC, excluding built-up area) within the  
367 boundary<sup>4,13,15</sup>. Thus, the SUHI intensity distribution maps for each new town and each period were constructed  
368 using two steps. (1) The SUHI intensity variation was calculated using equation (10):

$$\text{SUHI intensity distribution} = T_s - (T_{\text{mean}} + 0.5 \times \delta)_{\text{surrounding area}} \quad (10)$$

369 where  $T_s$  is the LST (°C) distribution of new town, and  $T_{\text{mean}}$  and  $\delta$  are the mean and standard deviation of LST  
370 in non-urban areas of new town. By subtracting the average temperature of non-urban areas from the  
371 temperature of the entire city, it may be verified that the actual SUHI effect was due to urban expansion, rather  
372 than the temporary LST value. In addition, the water bodies were excluded while calculating the SUHI intensity  
373 because it can irregularly influence the surface temperature (Lee et al, 2020). (2) The SUHI intensity variation  
374 was classified into six appropriate ranges: (i) value  $\leq 0$  °C, (ii)  $0$  °C < value  $\leq 2$  °C, (iii)  $2$  °C < value  $\leq 4$  °C, (iv)  
375  $4$  °C < value  $\leq 6$  °C, (v)  $6$  °C < value  $\leq 8$  °C, (vi)  $8$  °C < value. Thus, the difference in distribution and intensity  
376 of the SUHI phenomenon can be compared according to the change in LULC for each new town at each time  
377 period. In addition, classes are divided into value ranges, to facilitate future SUHI intensity distribution  
378 prediction using CA-Markov analysis. The indices, which were positively and negatively correlated with LST,  
379 were used to develop transition suitability maps for predicting the SUHI distribution. The normalised difference  
380 built-up index (NDBI) was used as the index that highly correlated with LST<sup>56</sup>. NDBI is the most widely  
381 accepted tool for the identification of built-up areas and has shown a high surface temperature correlation in  
382 previous studies<sup>13,22,57</sup>. The NDBI value was calculated using equation (11):

$$NDBI = \frac{SWIR - NIR}{SWIR + NIR} \quad (11)$$

383 Built-up areas are sensitive under the 1.55–1.75 wavelength range in the short-wave infrared (SWIR) band;  
 384 however, they are less sensitive under the 0.79–0.90 wavelength range in the NIR band<sup>58</sup>. The NDBI values  
 385 range from -1 to +1, and values near +1 generally represent highly dense built-up areas. Furthermore, NDVI was  
 386 used as the index that weakly correlated with LST. NDVI is the most common index for vegetation extraction  
 387 and has shown a strong negative correlation with LST in previous studies<sup>32,57,59</sup>. Fuzzy membership functions  
 388 were also used to standardise the factor maps to 0–1, where 0 represents a low SUHI potential and 1 represents a  
 389 high SUHI potential.

390

### 391 **Data availability**

392 Satellite images from 1989 to 2018 used in this study are freely available at <http://earthexplorer.usgs.gov/>. Other  
 393 datasets are available upon request from K. Lee (leedake@korea.ac.kr).

394

### 395 **References**

- 396 1. United Nations. The World's cities in 2018. *Department of Economic and Social Affairs, Population Division,*  
 397 *World Urbanization Prospects* 1–34 (2018).
- 398 2. Liping, C., Yujun, S., & Saeed, S. Monitoring and predicting land use and land cover changes using remote s  
 399 ensing and GIS techniques—A case study of a hilly area, Jiangle, China. *PloS One* **13(7)**, e0200493 (2018).
- 400 3. Eliasson, I. The use of climate knowledge in urban planning. *Landsc. Urban Plan.* **48(1–2)**, 31–44 (2000).
- 401 4. Lee, K., Kim, Y., Sung, H. C., Ryu, J., & Jeon, S. W. Trend analysis of urban heat island intensity according  
 402 to urban area change in Asian mega cities. *Sustain.* **12(1)**, 112 (2020).
- 403 5. Grimmond, S. U. Urbanization and global environmental change: local effects of urban warming. *Geogr. J.* **173(**  
 404 **1)**, 83–88 (2007).
- 405 6. Santamouris, M. Using cool pavements as a mitigation strategy to fight urban heat island—A review of the act  
 406 ual developments. *Renew. Sustain. Energy Rev.* **26**, 224–240 (2013).
- 407 7. Tran, H., Uchihama, D., Ochi, S., & Yasuoka, Y. Assessment with satellite data of the urban heat island effec  
 408 ts in Asian mega cities. *Int. J. Appl. Earth Obs. Geoinform.* **8(1)**, 34–48 (2006).
- 409 8. Clinton, N., & Gong, P. MODIS detected surface urban heat islands and sinks: Global locations and controls

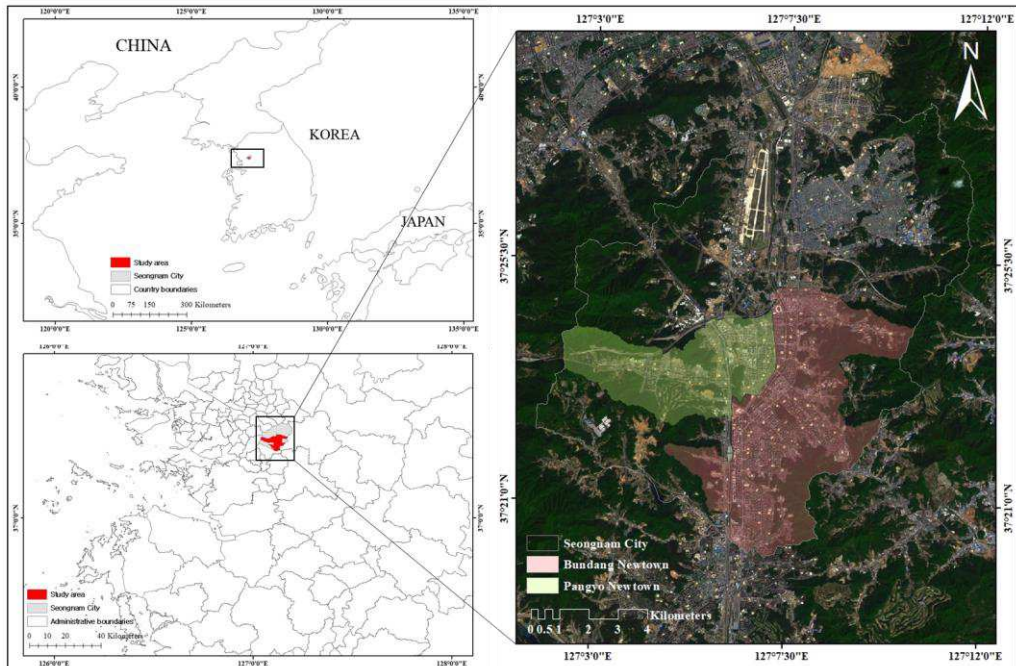
- 410 . *Remote Sens. Environ.* **134**, 294–304 (2013).
- 411 9. Voogt, J. A., & Oke, T. R. Thermal remote sensing of urban climates. *Remote Sens. Environ.* **86(3)**, 370–384 (
- 412 2003).
- 413 10. Khammar, G. Analysis the Environmental Impacts of Pardis New Town By TOPSIS Model. *Int. J. Manag. Sci.*
- 414 *Bus. Res.* **2(7)**, 134-141 (2013).
- 415 11. Wakeman, R.. *Practicing Utopia: An Intellectual History of the New Town Movement* Ch. 2 (University of Chi
- 416 cago Press, 2016).
- 417 12. Qaid, A., Lamit, H. B., Ossen, D. R., & Shahminan, R. N. R. Urban heat island and thermal comfort conditio
- 418 ns at micro-climate scale in a tropical planned city. *Energy Build.* **133**, 577–595 (2016).
- 419 13. Guha, S., Govil, H., Dey, A., & Gill, N. Analytical study of land surface temperature with NDVI and NDBI
- 420 using Landsat 8 OLI and TIRS data in Florence and Naples city, Italy. *Eur. J. Remote Sens.* **51(1)**, 667–678 (2
- 421 018).
- 422 14. Oke, T., *et al.* *Urban Climates* Ch. 7 (Cambridge University Press, 2017)
- 423 15. Zhou, B., Rybski, D., & Kropp, J. P. On the statistics of urban heat island intensity. *Geophys. Res. Lett.* **40(20)**
- 424 , 5486–5491 (2013).
- 425 16. Raymond, W. H., Rabin, R. M., & Wade, G. S. Evidence of an agricultural heat island in the lower Mississip
- 426 pi River floodplain. *Bull. Am. Meteorol. Soc.* **75(6)**, 1019–1026 (1994).
- 427 17. Huovila, P. *Buildings and Climate Change: Status, Challenges, and Opportunities* Ch. 1 (UNEP/Earthprint. 2007
- 428 ).
- 429 18. Li, Y., Schubert, S., Kropp, J. P., & Rybski, D. On the influence of density and morphology on the Urban H
- 430 eat Island intensity. *Nature Commun.* **11(1)**, 1–9 (2020).
- 431 19. Häkkinen, T., *et al.* *Methods and Concepts for Sustainable Renovation of Building* Ch. 4 (VTT Technical Resea
- 432 rch Centre of Finland: Espoo, Finland, 2012).
- 433 20. Yeh, S. W., *et al.* The record-breaking heat wave in 2016 over South Korea and its physical mechanism. *Mon.*
- 434 *Weather Rev.* **146(5)**, 1463–1474 (2018).
- 435 21. Nazeer, M., Nichol, J. E., & Yung, Y. K. Evaluation of atmospheric correction models and Landsat surface ref
- 436 lectance product in an urban coastal environment. *Int. J. Remote Sens.* **35(16)**, 6271–6291 (2014).
- 437 22. Saha, P., Bandopadhyay, S., Kumar, C., & Mitra, C. Multi-approach synergic investigation between land surfac
- 438 e temperature and land-use land-cover. *J. Earth Syst. Sci.* **129(1)**, 1–21 (2020).
- 439 23. Sun, J., Yang, J., Zhang, C., Yun, W., & Qu, J. Automatic remotely sensed image classification in a grid envi
- 440 ronment based on the maximum likelihood method. *Math. Computer Model.* **58(3–4)**, 573–581 (2013).
- 441 24. Wang, S. W., Munkhnasan, L., & Lee, W. K. Land use and land cover change detection and prediction in Bh
- 442 utan's high altitude city of Thimphu, using cellular automata and Markov chain. *Environmental Challenges.* **2**, 1

- 443 00017 (2020).
- 444 25. Al-Ahmadi, F. S., & Hames, A. S. Comparison of four classification methods to extract land use and land cov  
445 er from raw satellite images for some remote arid areas, Kingdom of Saudi Arabia. *Earth* **20(1)**, 167–191 (2009  
446 ).
- 447 26. Erbek, F. S., Özkan, C., & Taberner, M. Comparison of maximum likelihood classification method with superv  
448 ised artificial neural network algorithms for land use activities. *Int. J. Remote Sens.* **25(9)**, 1733–1748 (2004).
- 449 27. Yuan, D. A simulation comparison of three marginal area estimators for image classification. *Photogramm. Eng.*  
450 *Remote Sens.* **63(4)**, 385–391 (1997).
- 451 28. Lee, K., *et al.* The Integration of Remote Sensing and Field Surveys to Detect Ecologically Damaged Areas fo  
452 r Restoration in South Korea. *Remote Sens.* **12(22)**, 3687 (2020).
- 453 29. Congalton, R. G. A review of assessing the accuracy of classifications of remotely sensed data. *Remote Sens. E*  
454 *nviron.* **37(1)**, 35–46 (1991).
- 455 30. Avdan, U., & Jovanovska, G. Algorithm for automated mapping of land surface temperature using LANDSAT  
456 8 satellite data. *J. Sens.* **2016**, 1-8 (2016).
- 457 31. Artis, D. A., & Carnahan, W. H. Survey of emissivity variability in thermography of urban areas. *Remote Sens.*  
458 *Environ.* **12(4)**, 313–329 (1982).
- 459 32. Weng, Q., Lu, D., & Schubring, J. Estimation of land surface temperature–vegetation abundance relationship fo  
460 r urban heat island studies. *Remote Sens. Environ.* **89(4)**, 467–483 (2004).
- 461 33. Shen, H., Huang, L., Zhang, L., Wu, P., & Zeng, C. Long-term and fine-scale satellite monitoring of the urba  
462 n heat island effect by the fusion of multi-temporal and multi-sensor remote sensed data: A 26-year case study  
463 of the city of Wuhan in China. *Remote Sens. Environ.* **172**, 109–125 (2016).
- 464 34. Mallick, J., Singh, C. K., Shashtri, S., Rahman, A., & Mukherjee, S. Land surface emissivity retrieval based o  
465 n moisture index from LANDSAT TM satellite data over heterogeneous surfaces of Delhi city. *Int. J. Appl. Ea*  
466 *rth Obs. Geoinform.* **19**, 348–358 (2012).
- 467 35. Radhi, H., Fikry, F., & Sharples, S. Impacts of urbanisation on the thermal behaviour of new built up environ  
468 ments: A scoping study of the urban heat island in Bahrain. *Landsc. Urban Plan.* **113**, 47–61 (2013).
- 469 36. Sobrino, J. A., Jiménez-Muñoz, J. C., & Paolini, L. Land surface temperature retrieval from LANDSAT TM 5  
470 . *Remote Sens. Environ.* **90(4)**, 434–440 (2004).
- 471 37. Wang, F., *et al.* An improved mono-window algorithm for land surface temperature retrieval from Landsat 8 th  
472 ermal infrared sensor data. *Remote Sens.* **7(4)**, 4268–4289 (2015).
- 473 38. Sobrino, J. A., & Raissouni, N. Toward remote sensing methods for land cover dynamic monitoring: Applicatio  
474 n to Morocco. *Int. J. Remote Sens.* **21(2)**, 353–366 (2000).
- 475 39. Sekertekin, A., & Bonafoni, S. Land surface temperature retrieval from Landsat 5, 7, and 8 over rural areas: a

- 476 assessment of different retrieval algorithms and emissivity models and toolbox implementation. *Remote Sens.* **12**(2)  
 477 ), 294 (2020).
- 478 40. Yu, X., Guo, X., & Wu, Z. Land surface temperature retrieval from Landsat 8 TIRS—Comparison between rad  
 479 iative transfer equation-based method, split window algorithm and single channel method. *Remote Sens.* **6**(10), 9  
 480 829–9852 (2014).
- 481 41. Carlson, T. N., & Ripley, D. A. On the relation between NDVI, fractional vegetation cover, and leaf area inde  
 482 x. *Remote Sens. Environ.* **62**(3), 241–252 (1997).
- 483 42. Tucker, C. J. Red and photographic infrared linear combinations for monitoring vegetation. *Remote Sens. Environ.*  
 484 **8**(2), 127–150 (1979).
- 485 43. Kamusoko, C., Aniya, M., Adi, B., & Manjoro, M. Rural sustainability under threat in Zimbabwe—simulation o  
 486 f future land use/cover changes in the Bindura district based on the Markov-cellular automata model. *Appl. Geogr.* **29**(3), 435–447 (2009).
- 487
- 488 44. Keshtkar, H., & Voigt, W. A spatiotemporal analysis of landscape change using an integrated Markov chain an  
 489 d cellular automata models. *Model. Earth Syst. Environ.* **2**(1), 10 (2016).
- 490 45. Hamad, R., Balzter, H., & Kolo, K. Predicting land use/land cover changes using a CA-Markov model under t  
 491 wo different scenarios. *Sustain.* **10**(10), 3421 (2018).
- 492 46. Aaviksoo, K. Simulating vegetation dynamics and land use in a mire landscape using a Markov model. *Landsc.*  
 493 *Urban Plan.* **31**(1-3), 129–142 (1995).
- 494 47. Kumar, S., Radhakrishnan, N., & Mathew, S. Land use change modelling using a Markov model and remote s  
 495 ensing. *Geomat. Nat. Hazards Risk* **5**(2), 145–156 (2014).
- 496 48. Boerner, R. E., *et al.* Markov models of inertia and dynamism on two contiguous Ohio landscapes. *Geogr. Ana*  
 497 *l.* **28**(1), 56–66 (1996).
- 498 49. Brown, D. G., Walker, R., Manson, S., & Seto, K. Modeling land use and land cover change. In *Land change*  
 499 *science* (pp. 395–409). (Springer, Dordrecht, 2012).
- 500 50. Sang, L., Zhang, C., Yang, J., Zhu, D., & Yun, W. Simulation of land use spatial pattern of towns and villag  
 501 es based on CA–Markov model. *Math. Computer Model.* **54**(3–4), 938–943 (2011).
- 502 51. Myint, S. W., & Wang, L. Multicriteria decision approach for land use land cover change using Markov chain  
 503 analysis and a cellular automata approach. *Can. J. Remote Sens.* **32**(6), 390–404 (2006).
- 504 52. Anas, A., Arnott, R., & Small, K. A. Urban spatial structure. *J. Econ. Lit.* **36**(3), 1426–1464 (1998).
- 505 53. Hu, Z., & Lo, C. P. Modeling urban growth in Atlanta using logistic regression. *Computers Environ. Urban Syst.* **31**(6), 667–688 (2007).
- 506
- 507 54. Kasraian, D., Maat, K., & van Wee, B. The impact of urban proximity, transport accessibility and policy on u  
 508 rban growth: A longitudinal analysis over five decades. *Environ. Plan. B* **46**(6), 1000–1017 (2019).

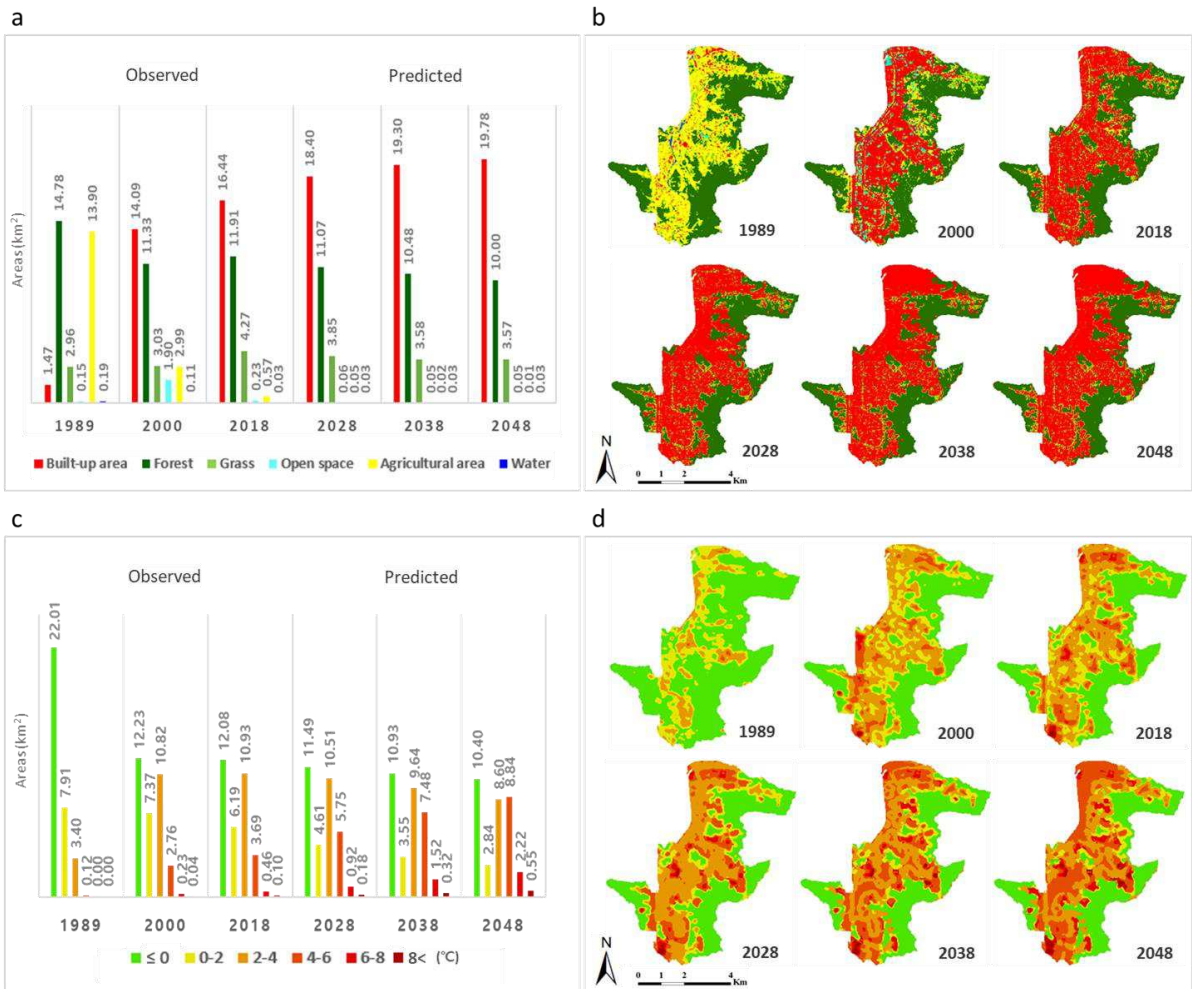
- 509 55. Kechebour, B. E. Relation between stability of slope and the urban density: case study. *Proced. Eng.* **114**, 824–  
510 831 (2015).
- 511 56. Zha, Y., Gao, J., & Ni, S. Use of normalized difference built-up index in automatically mapping urban areas f  
512 rom TM imagery. *Int. J. Remote Sens.* **24(3)**, 583–594 (2003).
- 513 57. Tariq, A., & Shu, H. CA-Markov Chain Analysis of Seasonal Land Surface Temperature and Land Use Land  
514 Cover Change Using Optical Multi-Temporal Satellite Data of Faisalabad, Pakistan. *Remote Sens.* **12(20)**, 3402 (  
515 2020).
- 516 58. Bhatti, S. S., & Tripathi, N. K. Built-up area extraction using Landsat 8 OLI imagery. *GIScience Remote Sens*  
517 . **51(4)**, 445–467 (2014).
- 518 59. Sun, H., Chen, Y., & Zhan, W. Comparing surface-and canopy-layer urban heat islands over Beijing using MO  
519 DIS data. *Int. J. Remote Sens.* **36(21)**, 5448–5465 (2015).
- 520 60. Yahia, M. W., Johansson, E., Thorsson, S., Lindberg, F., & Rasmussen, M. I. Effect of urban design on micro  
521 climate and thermal comfort outdoors in warm-humid Dar es Salaam, Tanzania. *International journal of biomete*  
522 *orology*, **62(3)**, 373-385 (2018).
- 523
- 524

525 **Figures with legends**



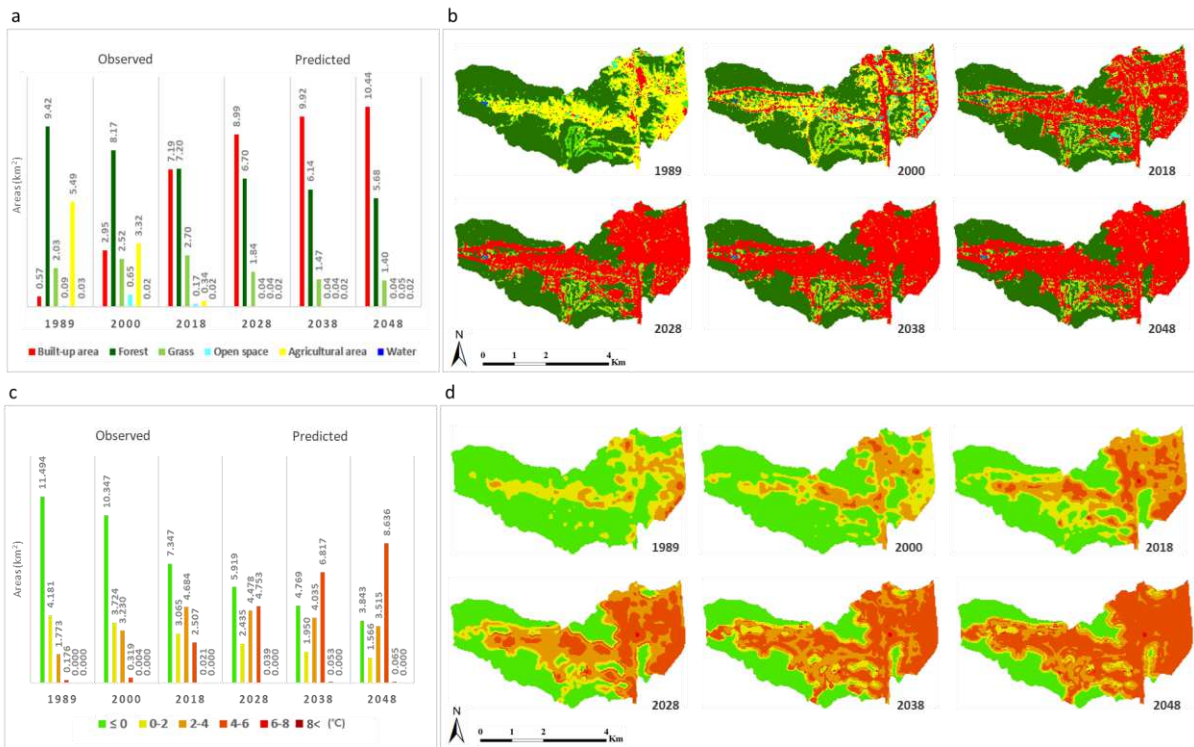
526

527 **Fig. 1 Map of study area. a.** Geographical location of the two new towns. **b.** Enlarged image showing the new  
528 towns. **c.** Landsat OLI image acquired on May 09, 2018.



529

530 **Fig. 2** SUHI distribution according to LULC changes from 1989 to 2048 in Bundang new town. **a.** Areas of  
 531 LULC in Bundang new town from 1989 to 2048. **b.** LULC maps of Bundang new town from 1989 to 2048. **c.**  
 532 Areas of SUHI distribution in Bundang new town from 1989 to 2048. **d.** SUHI distribution maps of Bundang new  
 533 town from 1989 to 2048.



534

535 **Fig. 3** SUHI distribution according to LULC changes from 1989 to 2048 in Pangyo new town. **a.** Areas of  
 536 LULC in Pangyo new town from 1989 to 2048. **b.** LULC maps of Pangyo new town from 1989 to 2048. **c.** Areas  
 537 of SUHI distribution in Pangyo new town from 1989 to 2048. **d.** SUHI distribution maps of Pangyo new town  
 538 from 1989 to 2048.

**Table 1.** Development plan features for each new town

<b>Division (unit)</b>	<b>Bundang new town</b>	<b>Pangyo new town</b>
Generation of New town	1 <sup>st</sup> generation	2 <sup>nd</sup> generation
Development period	1989–1996	2003–2017
Whole area (km <sup>2</sup> )	33.45	17.62
Development plan area (km <sup>2</sup> )	19.64	8.9
Number of household (thousands)	97.6	29.3
Population density (number/ha)	199	98
Average greenspace ratio (%)	12–25	25–35
Average floor space ratio (%)	184	161
Transportation infrastructure	Vehicle-oriented	Public transportation-oriented

540

541 **Acknowledgements**

542 This work was conducted with the support of the Korea Environment Industry & Technology Institute (KEITI)  
543 through its Urban Ecological Health Promotion Technology Development Project, and funded by the Korea  
544 Ministry of Environment (MOE) (2020002770003).

545 **Author contributions**

546 K. Lee, S.H. Kim, and S.W. Jeon: research design; H.C. Sung and Y. Kim: data collection; K. Lee, Y. Kim, and  
547 H.C. Sung: empirical analysis; K. Lee and S.H. Kim: manuscript draft; and all authors: result interpretation and  
548 writing the paper.

549 **Competing interests**

550 The authors declare no competing interests.

# Figures

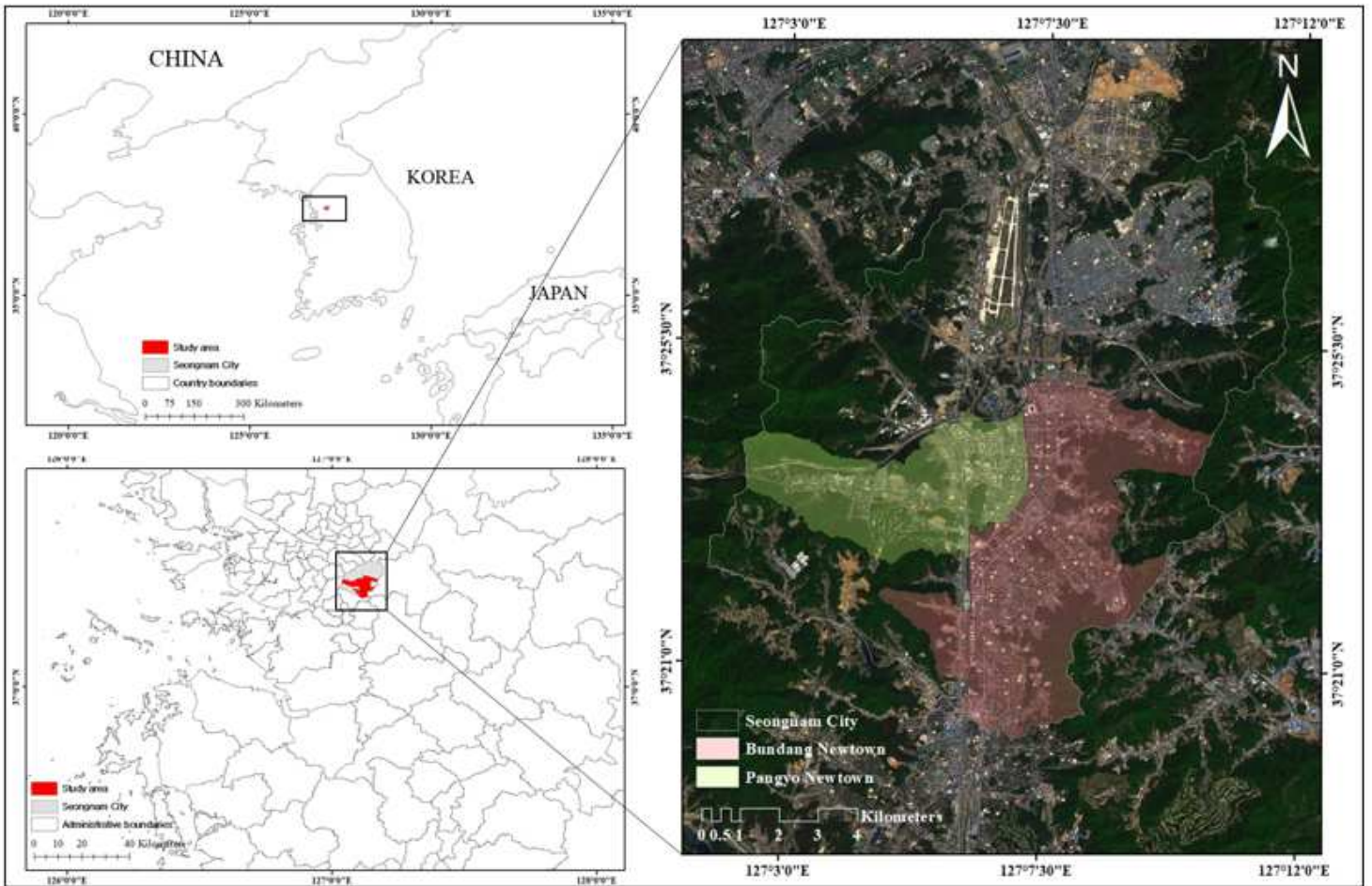


**Figure 1**

Map of study area. a. Geographical location of the two new towns. b. Enlarged image showing the new towns. c. Landsat OLI image acquired on May 09, 2018. Note: The designations employed and the presentation of the material on this map do not imply the expression of any opinion whatsoever on the part of Research Square concerning the legal status of any country, territory, city or area or of its authorities, or concerning the delimitation of its frontiers or boundaries. This map has been provided by the authors.

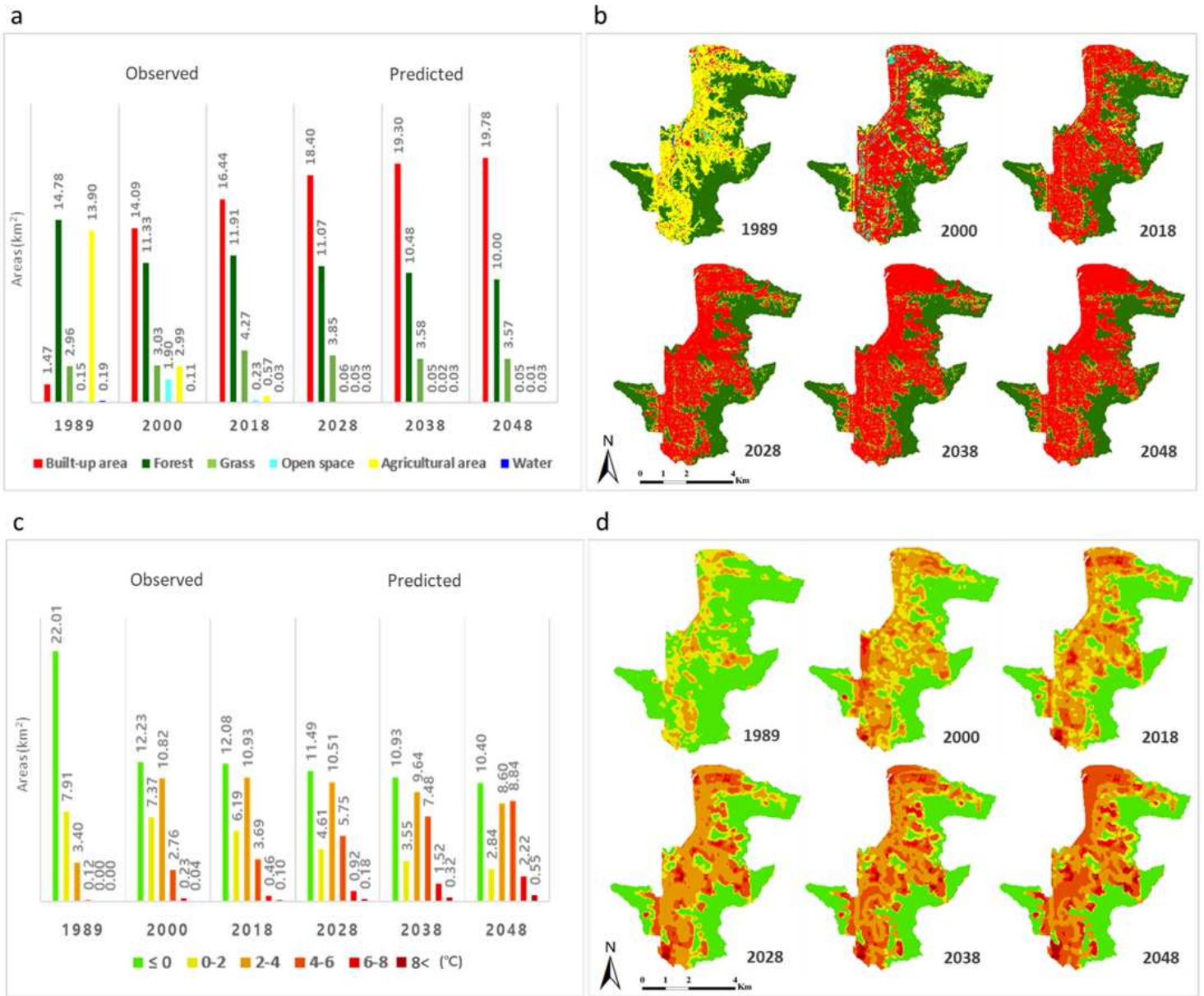


**Figure 2**

SUHI distribution according to LULC changes from 1989 to 2048 in Bundang new town. a. Areas of LULC in Bundang new town from 1989 to 2048. b. LULC maps of Bundang new town from 1989 to 2048. c. Areas of SUHI distribution in Bundang new town from 1989 to 2048. d. SUHI distribution maps of Bundang new town from 1989 to 2048. Note: The designations employed and the presentation of the material on this map do not imply the expression of any opinion whatsoever on the part of Research Square concerning the legal status of any country, territory, city or area or of its authorities, or concerning the delimitation of its frontiers or boundaries. This map has been provided by the authors.

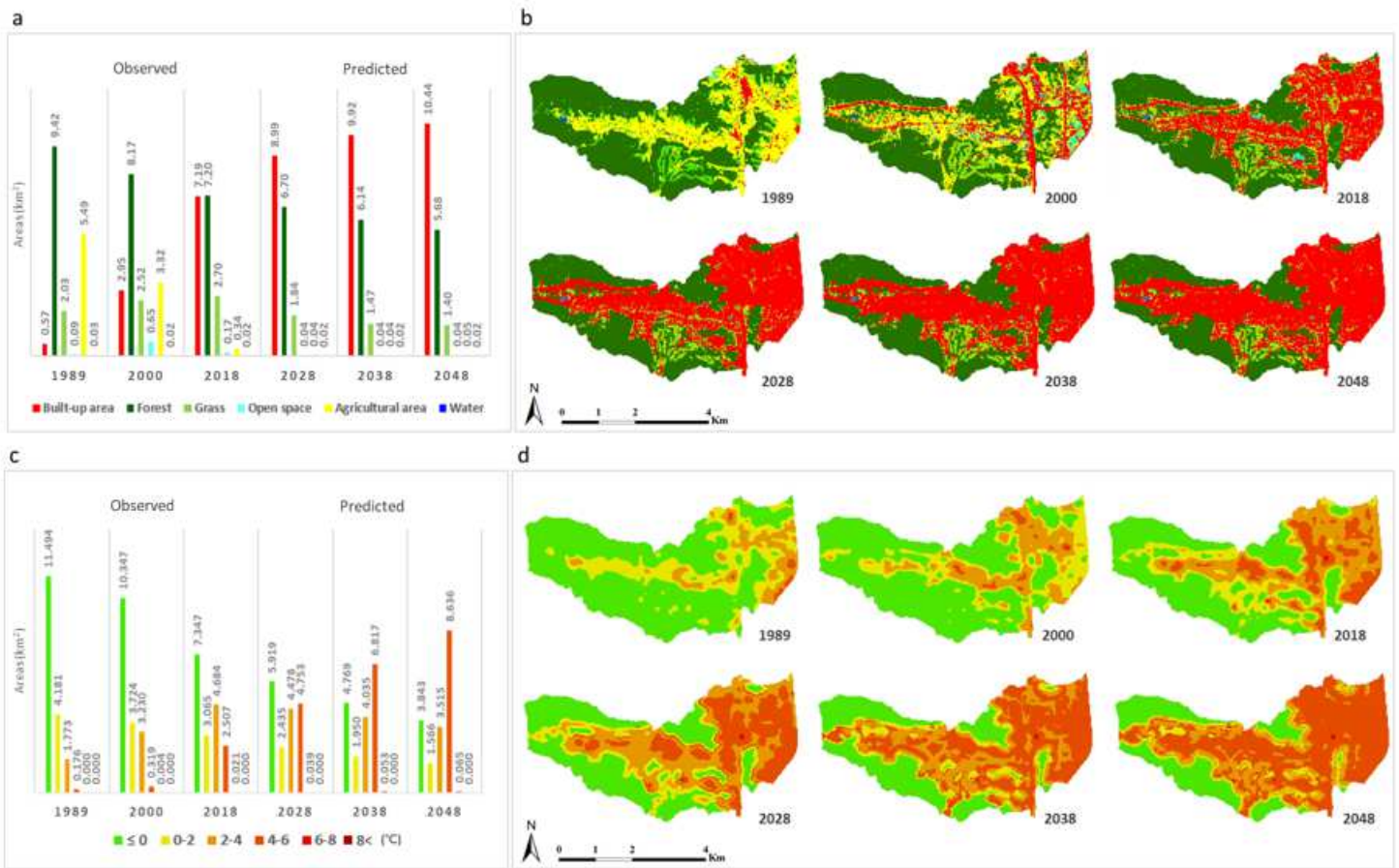


**Figure 3**

SUHI distribution according to LULC changes from 1989 to 2048 in Pangyo new town. a. Areas of LULC in Pangyo new town from 1989 to 2048. b. LULC maps of Pangyo new town from 1989 to 2048. c. Areas of SUHI distribution in Pangyo new town from 1989 to 2048. d. SUHI distribution maps of Pangyo new town from 1989 to 2048. Note: The designations employed and the presentation of the material on this map do not imply the expression of any opinion whatsoever on the part of Research Square concerning the legal status of any country, territory, city or area or of its authorities, or concerning the delimitation of its frontiers or boundaries. This map has been provided by the authors.